INTERNATIONAL JOURNAL FOR NUMERICAL METHODS IN ENGINEERING
Int. J. Numer. Meth. Engng 2009; **80**:320–337
Published online 28 April 2009 in Wiley InterScience (www.interscience.wiley.com). DOI: 10.1002/nme.2633

A boundary face method for potential problems in three dimensions

Jianming Zhang[*,†], Xianyun Qin, Xu Han and Guangyao Li

State Key Laboratory of Advanced Design and Manufacturing for Vehicle Body, College of Mechanical and Vehicle Engineering, Hunan University, Changsha 410082, China

SUMMARY

This work presents a new implementation of the boundary node method (BNM) for numerical solution of Laplace's equation. By coupling the boundary integral equations and the moving least-squares (MLS) approximation, the BNM is a boundary-type meshless method. However, it still uses the standard elements for boundary integration and approximation of the geometry, thus loses the advantages of the meshless methods. In our implementation, here called the boundary face method, the boundary integration is performed on boundary faces, which are represented in parametric form exactly as the boundary representation data structure in solid modeling. The integrand quantities, such as the coordinates of Gauss integration points, Jacobian and out normal are calculated directly from the faces rather than from elements. In order to deal with thin structures, a mixed variable interpolation scheme of 1-D MLS and Lagrange Polynomial for long and narrow faces. An adaptive integration scheme for nearly singular integrals has been developed. Numerical examples show that our implementation can provide much more accurate results than the BNM, and keep reasonable accuracy in some extreme cases, such as very irregular distribution of nodes and thin shells. Copyright © 2009 John Wiley & Sons, Ltd.

Received 24 November 2008; Revised 21 February 2009; Accepted 13 March 2009

KEY WORDS: meshless methods; boundary node method; moving least-squares approximation; boundary face method

1. INTRODUCTION

Meshless techniques to obtain numerical solutions for PDEs without resorting to an element frame have been popular throughout the computational mechanics community for the past two decades. This is because that, with mesh-based techniques as the finite element method (FEM) or the

[*] Correspondence to: Jianming Zhang, State Key Laboratory of Advanced Design and Manufacturing for Vehicle Body, College of Mechanical and Vehicle Engineering, Hunan University, Changsha 410082, China.
[†] E-mail: zhangjianm@gmail.com

Contract/grant sponsor: National Science Foundation of China; contract/grant numbers: 10725208, 60635020, 50625519

boundary element method (BEM), the task of mesh generation for complex geometries is often time-consuming and prone to errors, and the difficulties with re-meshing in problems involving moving boundaries, large deformations or crack propagation is crucial. Many kinds of meshless method have been proposed so far [1–10]. These methods can be simply sorted into two categories: the domain type and the boundary type. The domain-type meshless methods are represented by the element-free Galerkin method (EFG) [2] which uses a global symmetric weak form and the shape functions from the moving least-squares approximation. A feature of this method is that it uses a background cell structure for the 'energy' integration. Atluri and his co-workers have developed two meshless methods of domain type: the meshless local boundary integral equation (MLBIE) [3] and the meshless local Petrov-Galerkin (MLPG) approach [4]. Both methods use local weak form over local sub-domains, so that integrals can be evaluated over regularly shaped domains (for example, circles in 2-D problems and spheres in 3-D problems) and their boundaries. They called their method 'truly meshless method'.

The boundary-type meshless methods can be represented by the boundary node method (BNM) [5, 6] and the Hybrid Boundary Node Method (HdBNM) [7–10]. The BNM couples the moving least-squares (MLS) and the boundary integral equations (BIE), and uses background cells for boundary integration as the EFG, while the HdBNM combines the MLS interpolation scheme with the hybrid displacement variational formulation, and uses local form as the MLPG to avoid the use of background cells. However, the using of background cells should not be considered as a drawback of meshless methods if the background cells can be generated without much efforts. As a matter of fact, in 'truly meshless' methods, as each sub-domain usually includes only one node, the radius has to be properly chosen. To determine the radius of a sub-domain for a node, one has to calculate the distances between its neighboring nodes. This leads to a fact that generation of the sub-domains in many cases may need more work than background meshing. Therefore, the BNM may be a better option than the HdBNM for numerical solution of boundary value problems. Unfortunately, in the implementation of the BNM for 3-D cases [6], the authors did not use background cells but the standard elements of FEM or BEM to approximate geometry of the domain and performed the integration on these elements. In this paper, we present a new implementation of the BNM. In our implementation, here called the boundary face method (BFM), the boundary of the domain is represented by faces in parametric form exactly the same as the B-rep data structure in standard solid modeling packages. Both MLS and boundary integration are performed in the parametric spaces of the faces. For numerical integration, the faces are meshed with isoparametric lines and the geometric data, such as the coordinates of Gauss integration points, the Jacobian and the surface normal at the integration point are calculated directly from the face, and thus no geometric error is introduced. As the background cells can be so easily obtained, even easier than the sub-domains in the HdBNM, the new method can seamlessly interact with CAD packages, which is considered as a demanding feature for solving practical engineering problems by the computation research community [11].

Formulations of the MLS approximation on a generic surface are developed. To deal with thin shells, we have developed a mixed variable interpolation scheme of MLS and Lagrange Polynomial for variable interpolation on long and narrow faces and an adaptive integration scheme for nearly singular integrals. A number of numerical examples with various geometries are presented, in which computations are carried out with regular and irregular distribution of nodes. In addition, we have compared the present method with the BNM with regard to accuracy, convergence and the sensitivity of the results to the relative location of the source node in a cell. All results have shown very attractive features of the method.

DOI: 10.1002/nme

The paper is organized as follows. In Section 2, the MLS approximation on a generic 3-D surface and the mixed interpolation scheme on a long narrow face are described. Section 3 briefly describes the well-known BIE for potential problems. The adaptive face integration scheme is demonstrated in Section 4. Numerical examples for 3-D potential problems are given in Section 5. The paper ends with conclusions in Section 6.

2. THE MLS APPROXIMATION SCHEME ON A GENERIC 3-D SURFACE

An MLS interpolation scheme on a generic surface is proposed here. Since the nodes lie on the boundary $\partial\Omega$ of a 3-D body Ω in the BFM, the MLS approximation is only needed on the bounding surfaces. It is assumed that, for 3-D problems, the bounding surface $\partial\Omega$ of a 3-D body is the union of piecewise smooth segments called faces. The MLS interpolation is performed independently on each face, respectively, so that the discontinuity at edges and corners is avoided.

The first step for MLS interpolation on a generic surface is to choose a proper coordinate system. In most solid models, surfaces are represented in parametric forms:

$$x_1 = x_1(s_1, s_2), \quad x_2 = x_2(s_1, s_2), \quad x_3 = x_3(s_1, s_2) \tag{1}$$

where the parametric coordinates are defined in the range, $s_1, s_2 \in [0, 1]$. To make use of the B-rep data structure of the solid models, the MLS interpolation in this study is defined in the same parametric square. For problems in potential theory, the independent boundary variables are the potential and its normal gradient. These variables are also expressed in parametric forms as

$$\begin{aligned} u(x_1, x_2, x_3) &= u(x_1(s_1, s_2), x_2(s_1, s_2), x_3(s_1, s_2)) = u(s_1, s_2) \\ q(x_1, x_2, x_3) &\equiv \frac{\partial u}{\partial n} = q(x_1(s_1, s_2), x_2(s_1, s_2), x_3(s_1, s_2)) = q(s_1, s_2) \end{aligned} \tag{2}$$

where n is a unit outward normal to $\partial\Omega$ at the point (x_1, x_2, x_3).

Suppose a set of nodes $\{\mathbf{s}^I\}$, $I = 1, 2, \ldots, N$, are constructed on a face, the MLS interpolants $\tilde{u}$ and $\tilde{q}$ for u and q are defined by

$$\tilde{u}(\mathbf{s}) = \sum_{j=1}^{m} p_j(\mathbf{s}) a_j(\mathbf{s}) = \mathbf{p}^{\mathbf{T}}(\mathbf{s})\mathbf{a}(\mathbf{s}) \tag{3}$$

and

$$\tilde{q}(\mathbf{s}) = \sum_{j=1}^{m} p_j(\mathbf{s}) b_j(\mathbf{s}) = \mathbf{p}^{\mathbf{T}}(\mathbf{s})\mathbf{b}(\mathbf{s}) \tag{4}$$

where $\mathbf{s}$ is a field point with parametric coordinates (s_1, s_2), $p_1 = 1$ and $p_j(\mathbf{s})$, $j = 2, \ldots, m$ are monomials in (s_1, s_2). The monomials $p_j(\mathbf{s})$ provide the intrinsic polynomial bases for $\tilde{u}$ and $\tilde{q}$. In this study, a quadratic background basis is used, i.e.

$$\mathbf{p}^{\mathbf{T}}(\mathbf{s}) = [1, s_1, s_2, s_1^2, s_1 s_2, s_2^2], \quad m = 6 \tag{5}$$

The coefficient vectors $\mathbf{a}(\mathbf{s})$ and $\mathbf{b}(\mathbf{s})$ are determined by minimizing weighted discrete L_2 norms, defined as

$$J_1(\mathbf{s}) = \sum_{I=1}^{N} w_I(\mathbf{s})[\mathbf{p}^{\mathbf{T}}(\mathbf{s}^I)\mathbf{a}(\mathbf{s}) - \hat{u}_I]^2 \tag{6}$$

$$J_2(\mathbf{s}) = \sum_{I=1}^{N} w_I(\mathbf{s})[\mathbf{p}^{\mathbf{T}}(\mathbf{s}^I)\mathbf{b}(\mathbf{s}) - \hat{q}_I]^2 \tag{7}$$

It should be noted here that $\hat{u}_I$ and $\hat{q}_I, I = 1, 2, \ldots, N$ are simply parameters other than the nodal values of the unknowns $\tilde{u}_I$ and $\tilde{q}_I$ in general. This distinction between $\hat{u}_I$ and $\tilde{u}_I$ (or $\hat{q}_I$ and $\tilde{q}_I$) is very important because MLS interpolants lack the delta function property.

Solving for $\mathbf{a}(\mathbf{s})$ and $\mathbf{b}(\mathbf{s})$ by minimizing J_1 and J_2 in Equations (6) and (7), and substituting them into Equations (3) and (4) give a relation that can be written in the forms with interpolation functions similar to the shape functions in FEM:

$$\tilde{u}(\mathbf{s}) = \sum_{I=1}^{N} \Phi_I(\mathbf{s})\hat{u}_I \tag{8}$$

$$\tilde{q}(\mathbf{s}) = \sum_{I=1}^{N} \Phi_I(\mathbf{s})\hat{q}_I \tag{9}$$

where

$$\Phi_I(\mathbf{s}) = \sum_{j=1}^{m} p_j(\mathbf{s})[A^{-1}(\mathbf{s})B(\mathbf{s})]_{jI} \tag{10}$$

with matrices $A(\mathbf{s})$ and $B(\mathbf{s})$ defined by

$$A(\mathbf{s}) = \sum_{I=1}^{N} w_I(\mathbf{s})\mathbf{p}(\mathbf{s}^I)\mathbf{p}^{\mathbf{T}}(\mathbf{s}^I) \tag{11}$$

and

$$B(\mathbf{s}) = [w_1(\mathbf{s})\mathbf{p}(\mathbf{s}^1), w_2(\mathbf{s})\mathbf{p}(\mathbf{s}^2), \ldots, w_N(\mathbf{s})\mathbf{p}(\mathbf{s}^N)] \tag{12}$$

The MLS approximation is well defined only when the matrix A in Equation (11) is non-singular.

The $\Phi_I(\mathbf{s})$ is usually called the shape function of the MLS approximation corresponding to the nodal point $\mathbf{s}^I$. From Equations (10) and (12), it is seen that $\Phi_I(\mathbf{s}) = 0$ when $w_I(\mathbf{s}) = 0$. The fact that $\Phi_I(\mathbf{s})$ vanishes for $\mathbf{s}$ not in the support of nodal point $\mathbf{s}^I$ preserves the local character of the MLS approximation.

The partial derivatives of $\Phi_I(\mathbf{s})$ are obtained as in Reference [2] to be

$$\Phi_{I,k} = \sum_{j=1}^{m} [p_{j,k}(A^{-1}B)_{jI} + p_j(A^{-1}B_{,k} + A^{-1}_{,k}B)_{jI}] \tag{13}$$

in which $A^{-1}_{,k} = (A^{-1})_{,k}$ represents the derivative of the inverse of A with respect to $s_k, k = 1, 2$, given by

$$A^{-1}_{,k} = -A^{-1}A_{,k}A^{-1} \tag{14}$$

where, $()_{,k}$ denotes $\partial()/\partial s_k$.

DOI: 10.1002/nme

In implementing the MLS approximation, the weight functions should be chosen at first. Several kinds of weight functions can be found in the literatures; the choice of weight functions and the consequences of a choice are discussed in detail elsewhere [3]. In this study, we use the Gaussian weight function. The Gaussian weight function corresponding to a node $\mathbf{s}^I$ can be written by

$$w_I(\mathbf{s})=\begin{cases}\dfrac{\exp[-(d_I/c_I)^2]-\exp[-(\hat{d}_I/c_I)^2]}{1-\exp[-(\hat{d}_I/c_I)^2]}, & 0\leqslant d_I\leqslant\hat{d}_I\\[2ex] 0, & d_I\geqslant\hat{d}_I\end{cases}\tag{15}$$

where c_I is a constant controlling the shape of the weight function, and $\hat{d}_I$ is the size of the support for the weight function w_I. It can be seen from the above equation that the weight function has a compact support determined by the parameter $\hat{d}_I$. The compact support is also an associated range of influence of each node. In the past, the shape of the compact support is usually chosen to be circle in meshless literatures, while in this study, we choose ellipse for the shape of the compact support with $\hat{d}_I$ being the half-length of major axis of the ellipse. Denoting the half-length of minor axis by $\hat{d}'_I$, we have the following expression for d_I:

$$d_I=\sqrt{(s_1-s_1^I)^2+\frac{\hat{d}_I^2}{\hat{d}_I'^2}(s_2-s_2^I)^2}\tag{16}$$

In order to ensure the regularity of A, the $\hat{d}_I$ and $\hat{d}'_I$ should be chosen in such a way that they are large enough to have a sufficient number of nodes which are covered in the domain of definition of every sample point ($N\geqslant m$). But too large $\hat{d}_I$ and $\hat{d}'_I$ will lose the local character of the MLS interpolation, or even lead to an ill-conditioned matrix A. In this study, $\hat{d}_I$ and $\hat{d}'_I$ are chosen such that $4m$–$8m$ nodes are included in the support of a node.

However, even if the condition ($N\geqslant m$) is satisfied, but the N nodes in the domain of dependence of the sample point lie on a straight line on the face, then the matrix A becomes singular. This indicates that the MLS is not applicable to narrow strip surfaces, which exist in many thin shell structures. To handle this problem, we proposed a mixed interpolation scheme of 1-D MLS and Lagrange polynomial. Here take a strip surface as an example, which is assumed thin in the s_1 direction and long in the s_2 direction. We construct k ($3\geqslant k\geqslant 1$, and determined by the width of the strip) rows of nodes on the strip in the s_2 direction. The coordinate of s_1 and the number of nodes of each row are s_1^k and $N_k(N_k\geqslant 4)$, respectively. Then the potential u at a point $\mathbf{s}(s_1,s_2)$ can be interpolated by Lagrange polynomials in the s_1 direction:

$$\tilde{u}(\mathbf{s})=\sum_{j=1}^{k} l_{n,j}(s_1)\tilde{u}^j(s_2)\tag{17}$$

where $l_{n,j}(s_1)=\prod_{j\neq i}((s_1-s_1^j)/(s_1^i-s_1^j)), \tilde{u}^j(s_2)$ can be obtained by 1-D MLS approximation within each row of nodes independently, using the following formula:

$$\tilde{u}^j(s_2)=\sum_{I=1}^{N_k}\phi_I(s_2)\hat{u}_I^k\tag{18}$$

here, $\phi_I(s_2)$ is the shape function of the 1-D MLS approximation. For 1-D MLS and its derivative, please refer References [5, 7].

DOI: 10.1002/nme

For a face that is small in size in both directions, and thus the numbers of nodes distributed in the two directions are both less than 4, we interpolate the variables by Lagrange polynomials in two directions. In this case, actually, the face degenerates to a constant, a linear or a quadratic element of the standard BEM.

3. BOUNDARY INTEGRAL EQUATIONS AND DISCRETIZATIONS

The potential problem in three dimensions governed by Laplace's equation with boundary conditions is written as

$$\begin{aligned} u_{,ii} &= 0 \quad \forall x \in \Omega \\ u &= \bar{u} \quad \forall x \in \Gamma_u \\ u_{,i} n_i &\equiv q = \bar{q} \quad \forall x \in \Gamma_q \end{aligned} \tag{19}$$

where the domain Ω is enclosed by $\Gamma = \Gamma_u + \Gamma_q, \bar{u}$ and $\bar{q}$ are the prescribed potential and the normal flux, respectively, on the essential boundary Γ_u and on the flux boundary Γ_q, and n is the outward normal direction to the boundary Γ, with components $n_i, i = 1, 2, 3$.

The problem can be recast into an integral equation on the boundary. The well-known self-regular BIE for potential problems in 3-D is

$$0 = \int_\Gamma (u(\mathbf{s}) - u(\mathbf{y})) q^s(\mathbf{s}, \mathbf{y}) \, d\Gamma - \int_\Gamma q(\mathbf{s}) u^s(\mathbf{s}, \mathbf{y}) \, d\Gamma \tag{20}$$

where $q = \partial u / \partial n, \mathbf{y}$ is the source point and $\mathbf{s}$ the field point on the boundary. $u^s(\mathbf{s}, \mathbf{y})$ and $q^s(\mathbf{s}, \mathbf{y})$ are the fundamental solutions. For 3-D potential problems,

$$u^s(\mathbf{s}, \mathbf{y}) = \frac{1}{4\pi} \frac{1}{r(\mathbf{s}, \mathbf{y})} \tag{21}$$

$$q^s(\mathbf{s}, \mathbf{y}) = \frac{\partial u^s(\mathbf{s}, \mathbf{y})}{\partial n} \tag{22}$$

with r being the Euclidean distance between the source and field points.

The MLS interpolations or the mixed interpolations derived in Section 2 will be used to approximate u and q on the boundary Γ. The bounding surface is discretized into cells by isoparametric lines face by face. Substituting Equations (8) and (9) into Equation (20) and dividing Γ into N_c cells, we have

$$0 = -\sum_{j=1}^{N_c} \int_{\Gamma_j} q^s(\mathbf{s}, \mathbf{y}) \sum_{I=1}^{N} (\Phi_I(\mathbf{s}) - \Phi_I(\mathbf{y})) \hat{u}_I \, d\Gamma + \sum_{j=1}^{N_c} \int_{\Gamma_j} u^s(\mathbf{s}, \mathbf{y}) \sum_{I=1}^{N} \Phi_I(\mathbf{s}) \hat{q}_I \, d\Gamma \tag{23}$$

where $\Phi_I(\mathbf{y})$ and $\Phi_I(\mathbf{s})$ are the contributions from the Ith node to the collocation point $\mathbf{y}$ and field point $\mathbf{s}$, respectively. The first term on the right side of Equation (23) is regular in any case. Therefore, regular Gaussian integration can be used to evaluate it over each cell. However, special integration techniques are required for the second term, since it will become weakly singular as $\mathbf{s}$ approaches $\mathbf{y}$. When $\mathbf{y}$ and $\mathbf{s}$ belong to the same cell, the cell is treated as a singular cell and the special techniques developed in the next section are used to carry out the integration.

DOI: 10.1002/nme

Our integration scheme is different from that developed by Chati and Mukherjee [6] and may provide better accuracy. This is because we carry out the integrations directly in the parametric space of a face other than over elements, and thus no geometric error will be introduced.

Even when **y** and **s** belong to different cells, they can still be very close to each other. In this case, the second term on the right side of Equation (23) becomes nearly-singular. This case occurs when thin structures are involved and when the distribution of nodes is very irregular. We have also developed an adaptive scheme to calculate nearly singular integrals in the next section.

Equation (23) can be put in a matrix form as

$$\mathbf{H}\hat{\mathbf{u}}-\mathbf{G}\hat{\mathbf{q}}=\mathbf{0} \tag{24}$$

where $\hat{\mathbf{u}}$ and $\hat{\mathbf{q}}$ contain the approximations to the nodal values of u and q at the boundary nodes. A well-posed boundary value problem can be solved using Equation (24). However, transformations between $\hat{u}_I$ and $\tilde{u}_I, \hat{q}_I$ and $\tilde{q}_I$ is necessary because the MLS interpolants lack the delta function property of the usual BEM shape functions as mentioned in Section 2. For the panels where $\tilde{u}$ is prescribed, $\hat{u}_I$ is related to $\bar{u}_I$ by

$$\hat{u}_I=\sum_{J=1}^{N} R_{IJ}\tilde{u}_J=\sum_{J=1}^{N} R_{IJ}\bar{u}_J \tag{25}$$

and for the panels where $\tilde{q}$ is prescribed, $\hat{q}_I$ is related to $\bar{q}_I$ by

$$\hat{q}_I=\sum_{J=1}^{N} R_{IJ}\tilde{q}_J=\sum_{J=1}^{N} R_{IJ}\bar{q}_J \tag{26}$$

where $R_{IJ}=[\Phi_J(\mathbf{s}^I)]^{-1}$.

The computational efficiency of the proposed method in comparison with 3D domain schemes, e.g. FEM or EFG, is similar to that of BEM. Actually, considering a 3D mesh with n^3 nodes, the number of boundary nodes is around n^2, both the operation count and the memory requirements for the buildup of matrix equation (24) are of the order $O(n^4)$. The operation count increases to $O(n^6)$ if we attempt to solve the equation with conventional direct solvers such as Gaussian elimination. Therefore, although the dimensionality of a problem at hand is reduced by one, it is less computationally efficient than domain schemes. However, the proposed method significantly reduces the human-labor cost of introducing geometric meshes in complex-shaped structures, which is the aim of the development of a new class of computer methods, the so-called *meshless* or *element-free* methods. Moreover, the computational efficiency of the BFM can be enhanced dramatically if it is combined with the fast multipole method (FMM) [12–14].

4. WEAKLY AND NEARLY SINGULAR INTEGRATION SCHEMES

4.1. Weakly singular integration

The second term on the right side of Equation (23) becomes a weakly singular integral when **y** and **s** belong to a same cell, and the cell is treated as a singular cell. There have been various methods proposed in the past to handle weakly singular integrals arising in BEM. Chati and Mukherjee have used a method suggested by Nagaranjan and Mukherjee [15] to carry out the weakly singular integration in BNM. Here we propose a new method without using elements. The details follow.

DOI: 10.1002/nme

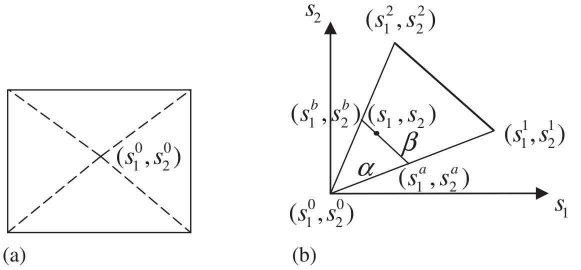

Figure 1. Weakly singular integration on a cell: (a) cell subdivision and (b) coordinate transformation.

All the cells in BFM are rectangular in shape in the parametric space, because we use isoparametric lines of a face to mesh the face into cells. Consider the weakly singular integral over a cell as shown in Figure 1(a). This can be represented as

$$I = \int_{\text{cell}} O(1/r)\,\mathrm{d}\Gamma \tag{27}$$

Now, the rectangular cell is divided into four triangles in the parametric space. For each triangles, the following mapping is used (see Figure 1(b)):

$$\begin{aligned} s_1^a &= s_1^0 + (s_1^1 - s_1^0)\alpha \\ s_2^a &= s_2^0 + (s_2^1 - s_2^0)\alpha \end{aligned} \tag{28a}$$

$$\begin{aligned} s_1^b &= s_1^0 + (s_1^2 - s_1^0)\alpha \\ s_2^b &= s_2^0 + (s_2^2 - s_2^0)\alpha \end{aligned} \tag{28b}$$

$$\begin{aligned} t_1 &= t_1^a + (t_1^b - t_1^a)\beta \\ t_2 &= t_2^a + (t_2^b - t_2^a)\beta \end{aligned} \qquad \alpha, \beta \in [0, 1] \tag{28c}$$

Then the integral I can be written as

$$I = \sum_{i=1}^{4} \int_0^1 \int_0^1 O(1/r) J_S(\mathbf{s}) J_L^{(i)}(\alpha)\,\mathrm{d}\alpha\,\mathrm{d}\beta \tag{29}$$

where J_S is the Jacobian of the face, $J_L^{(i)} = \alpha S_\Delta$ and

$$S_\Delta = |s_1^1 s_2^2 + s_1^2 s_2^0 + s_1^0 s_2^1 - s_1^2 s_2^1 - s_1^0 s_2^2 - s_1^1 s_2^0| \tag{30}$$

which is the area of the triangle in the parametric space, and keeps constant over the triangle. Now, regular Gaussian integration can be used to evaluate the above integral I. Since the mapping and the Jacobian are simpler than that of the method used by Chati and Mukherjee [6], our method may be computationally more efficient. Moreover, because we do not use elements to approximate the surface, no geometric error is introduced.

DOI: 10.1002/nme

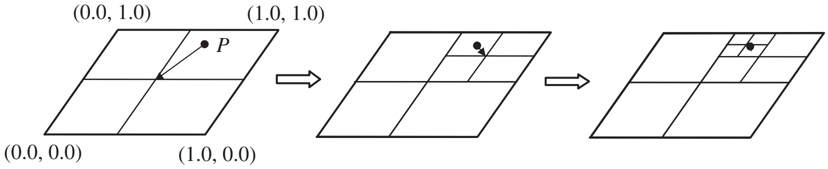

Figure 2. Subdivision of a cell in parametric space corresponding to a source point P.

4.2. *Nearly singular integration*

Nearly singularities arise in the BIE when slender or thin structures are considered and in cases where the boundary node distribution on a surface is very irregular, namely the densities of nodes along the two directions in parametric space are very different. Accurate evaluation of nearly singular integrals is a demanding task for successful implementation of BIE analyses. So far many techniques for dealing with nearly singular integrals have been proposed [16, 17]. Some of them are effective but involve complicated mathematic transformations of the integrals for a specific fundamental solution. To provide a general approach that is independent of the problem to be solved, here we developed an adaptive integration scheme based on the cell subdivision method. In this scheme, we first calculate the diagonal length of the integration cell, l, and the distance between the source point and the center of the cell, d, in the real-world-coordinate system. If l is smaller than d, this cell is taken as a regular integration patch, or it is divided into four equal subcells (see Figure 2). Then for each subcell, we repeat the above procedure until all patches become regular. Finally, using Gaussian quadrature for all patches, we can evaluate the integrals in Equation (23) very accurately even when the source point is very close to the integration cells. It should be pointed out that the patches are not like the elaborately constructed elements in the BEM and FEM. The subdivided patches of a same cell change for different source points. They can be easily constructed in the parametric space. Therefore, using these patches does not affect the fact that the BFM is a meshless method.

5. ILLUSTRATIVE NUMERICAL RESULTS

The current method has been tested thoroughly for three types of 3-D geometrical objects: a sphere, a cube, and an elbow pipe. To compare the current method with the BNM, the former two models are taken from Reference [6]. And the last one, a more geometrically complicated one, is added to show the advantage of the meshless nature of the present method. In order to assess the accuracy of the present method, we have used the following three analytical fields, which are also taken from [6]:

(i) *Linear solution*:

$$u=x+y+z \tag{31}$$

(ii) *Quadratic solution-1*:

$$u=xy+yz+zx \tag{32}$$

(iii) *Quadratic solution-2*:

$$u=-2x^2+y^2+z^2 \tag{33}$$

(iv) *Cubic solution*:

$$u=x^3+y^3+z^3-3yx^2-3xz^2-3zy^2 \tag{34}$$

In all cases, Laplace's equation $\nabla^2 u=0$ is solved, together with appropriately prescribed boundary conditions corresponding to the above analytical solutions.

For the purpose of error estimation and convergence study, a 'global' L_2 norm error, normalized by $|v|_{\max}$ is defined as follows [6]:

$$e=\frac{1}{|v|_{\max}}\sqrt{\frac{1}{N}\sum_{i=1}^{N}(v_i^{(e)}-v_i^{(n)})^2} \tag{35}$$

where $|v|_{\max}$ is the maximum value of u or q over N sample points, the superscripts (e) and (n) refer to the exact and numerical solutions, respectively.

In all computations, unless indicated otherwise, the support size of the weight function, $\hat{d}_I$ in Equation (15), is taken to be $4.0h$, with h being the minimum distance between the neighboring points, and the parameter c_I is taken to be such that $\hat{d}_I/c_I$ is constant and equal to 4.0.

5.1. Dirichlet problems on a sphere

The first example considers problems in a sphere of radius 2 unit, centered at the origin. The usual spherical polar coordinates θ and ϕ are used. The linear, quadratic and cubic fields (Equations (31)–(34)) are used as exact solutions. In each case, the Dirichlet boundary conditions corresponding to the exact solutions are imposed on the surface of the sphere. The results have been obtained for three sets of nodes: (a) 74 nodes, (b) 143 nodes, and (c) 286 nodes. The L_2 errors of nodal values of q, evaluated using Equation (35), for different sets of nodes and fields are shown in Figure 3. It can be seen that our method yields very accurate results and have high convergence rate. Figures 4 and 5 show variation in the potential and its directional derivative at locations inside the sphere. The results are obtained using 74 nodes. The gradient is dotted with the diagonal $(x=y=z)$ in order to get the directional derivative along this line. Values of u and q, at internal points that are close to the surface of the body, are calculated by the nearly singular integration scheme described in Section 4.1. It is seen that results are accurate even when the points are very close to the boundary.

It has been observed in BNM that the choice of the locations of the collocation nodes on each cell is an important ingredient for successful implementation of BNM. To compare with the BNM, we have also studied the influence of the locations of the collocation nodes on the accuracy of the BFM. In this study, the location of the collocation node on a cell is determined by a parameter $\alpha, 0\leqslant\alpha\leqslant 1$, using the following equation:

$$\mathbf{s}_P=\mathbf{s}_{\mathrm{L}}+\alpha(\mathbf{s}_{\mathrm{R}}-\mathbf{s}_{\mathrm{L}})/2 \tag{36}$$

where, $\mathbf{s}_P$ is the collocation point, $\mathbf{s}_{\mathrm{L}}$ and $\mathbf{s}_{\mathrm{R}}$ are the lower-left and the upper-right corner points, respectively. Obviously, the collocation point is at the center of the cell when $\alpha=1$ and at the lower-left corner of the cell when $\alpha=0$. Computations have been performed for all the analytical

DOI: 10.1002/nme

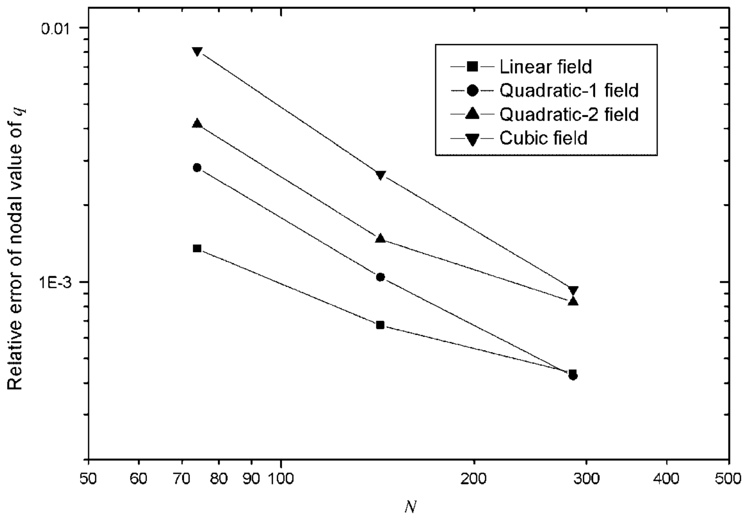

Figure 3. Relative errors and convergence rates for Dirichlet problem on a sphere. N is the number of nodes (one node per cell is used in the BFM).

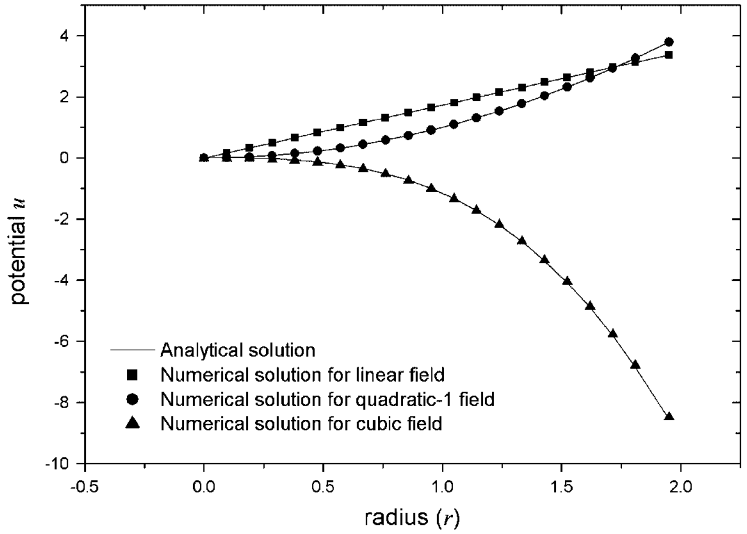

Figure 4. Variation in potential u along the line $x = y = z$ for a sphere.

fields using 74 nodes. The L_2 errors in q for various values of α are presented in Table I. Comparing with the Table I in Reference [6], it can be found that the accuracy of our method is much less sensitive to the relative location of the collocation point in a cell than that of the BNM. When α takes the values of 0.1, 0.5, and 1, the locations of the collocation points in the cells are shown in Figure 6.

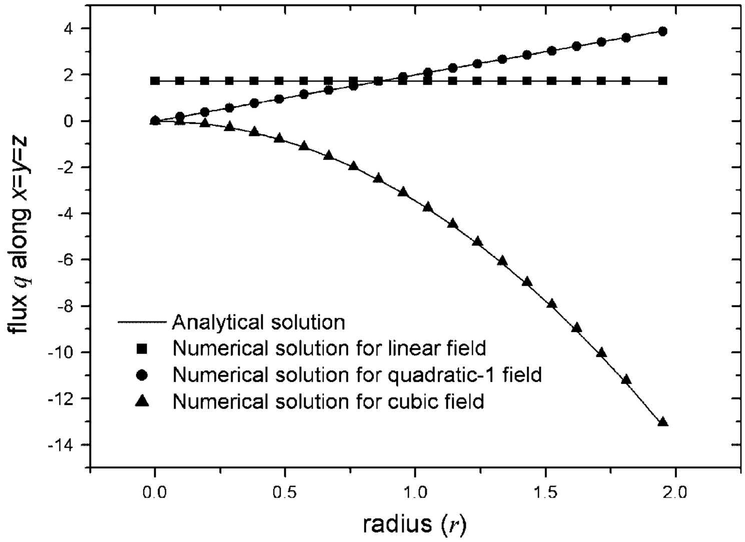

Figure 5. Variation of directional derivative of potential u along the line $x=y=z$ for a sphere.

Table I. Variation in L_2 error in q for Dirichlet problems on a sphere for various locations of the collocation point in the parent space.

α	$u=$linear (%)	$u=$quadratic-1 (%)	$u=$quadratic-2 (%)	$u=$cubic (%)
0.05	0.420	1.219	1.399	4.042
0.1	0.317	0.886	0.566	2.786
0.2	0.262	0.572	0.511	1.562
0.3	0.214	0.445	0.476	1.021
0.4	0.173	0.375	0.458	0.833
0.5	0.153	0.322	0.447	0.742
0.6	0.145	0.292	0.444	0.608
0.7	0.140	0.250	0.447	0.617
0.8	0.127	0.210	0.391	0.807
0.9	0.131	0.238	0.385	0.914
1.0	0.135	0.281	0.416	0.814

As in Reference [6], our method has also been tried on a more challenging problem which cannot be described by polynomial approximations. The exact solution of this problem is

$$u=\frac{2r^2}{R^2}\cos^2\phi-\frac{2r^2}{3R^2}-\frac{1}{3} \tag{37}$$

where R is the radius of the sphere and ϕ is the angle measured from the z-axis. The Dirichlet boundary condition on the surface then becomes

$$u|_{(r=R)}=\cos 2\phi \tag{38}$$

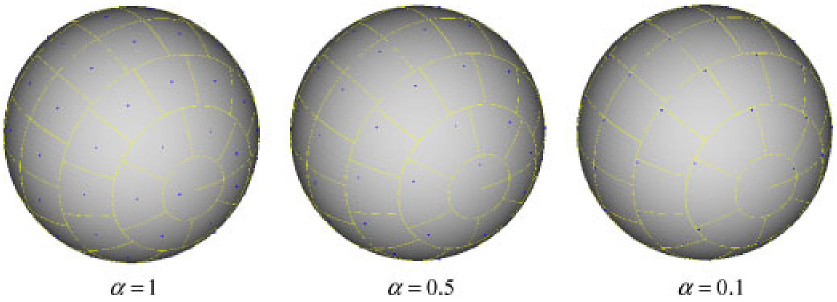

Figure 6. Relative locations of the collocation points in cells for various values of α.

Table II. Variation in L_2 error in q for Dirichlet problems on a cube for various locations of the collocation point in the parent space.

α	$u=$linear (%)	$u=$quadratic-1 (%)	$u=$quadratic-2 (%)	$u=$cubic (%)
0.05	0.420	1.219	1.399	0.937
0.1	0.317	0.886	0.566	0.928
0.2	0.262	0.572	0.511	1.000
0.3	0.214	0.445	0.476	0.897
0.4	0.173	0.375	0.458	0.748
0.5	0.153	0.322	0.447	0.606
0.6	0.145	0.292	0.444	0.485
0.7	0.140	0.250	0.447	0.387
0.8	0.127	0.210	0.391	0.313
0.9	0.131	0.238	0.385	0.261
1.0	0.135	0.281	0.416	0.243

Results are obtained with 74 nodes. The global L_2 error for q is 0.114%, which is nearly half of that obtained by the BNM.

5.2. *Dirichlet and mixed problems on a cube*

The case of the field for a $2\times2\times2$ cubic domain governed by Laplace's equation is presented as the second example. The cube faces are $x=\pm1, y=\pm1$, and $z=\pm1$, respectively. As in the first example, Equations (31)–(34) are used as the exact solutions. Dirichlet problems are solved for which the essential boundary conditions are imposed on all faces corresponding to the exact solutions. The 6×6 nodes on each face are used. Results have been obtained for various locations of the collocation points in the cells. The L_2 errors of nodal values of q with variation in α are presented in Table II. Again, in strong contrast with the results in Reference [6], the accuracy of our method is not dependent on the choice of the locations of the collocation points. In all cases, even when the collocation points are very close to the corners of the cells, our method has yielded satisfactory results.

A boundary value problem with mixed boundary conditions has also been solved. The quadratic-2 solution has been used here. The essential boundary conditions are imposed on faces $x=\pm1$ of the cube and the natural boundary conditions on faces $y=\pm1$ and $z=\pm1$. The numerical results have

DOI: 10.1002/nme

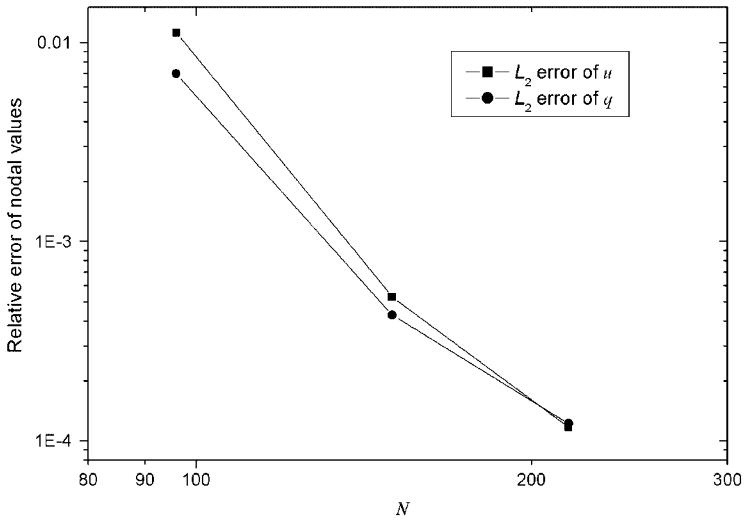

Figure 7. Relative errors of u and q and convergence rate for Dirichlet problem on a cube.

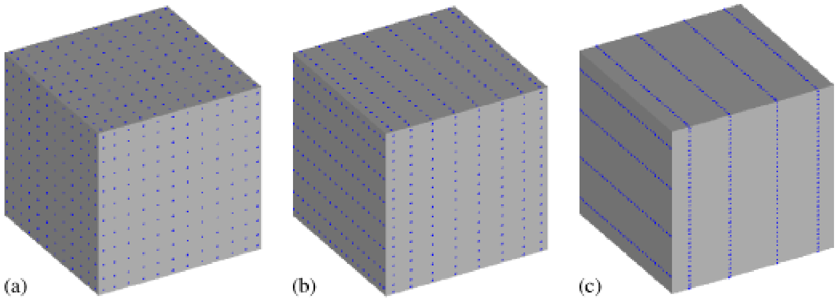

Figure 8. Node distributions on a cube: (a) 12×12 regular nodes; (b) 8×18 irregular nodes; and (c) 4×36 irregular nodes.

been obtained using three sets of nodes: (a) 4×4 nodes on each face (totally 96 cells), (b) 5×5 nodes on each face (totally 150 cells), and (c) 6×6 nodes on each face (totally 216 cells). Figure 7 shows the L_2 errors of nodal values of u and q when different numbers of nodes are used. It can be clearly seen that excellent results have been obtained and high convergence rates achieved.

In order to understand the effect of node distribution on the accuracy of the obtained results, a new case has been studied. In the case study, totally 864 nodes are used, of which three spacing patterns on each face are considered: (a) 12×12 regular distribution, (b) 8×18 irregular distribution, and (c) 4×36 very irregular distribution. The node distributions are shown in Figure 8. The analytical fields expressed by Equations (31)–(34) have been tested. The L_2 errors of nodal values for q (denoted by Err_q) and time required for constructing the coefficient matrices (denoted by Mat_t) and solving the equation (denoted by Sol_t) are presented in Table III. The results obtained with the meshes (a) and (b) are very accurate. Even for the very irregular mesh (c), the results are

Table III. Variation in L_2 error of q for Dirichlet problems on a cube for different node spacing patterns and timing results.

	Node spacing	12×12	8×18	4×36
$u=$linear	Err_q (%)	0.04226	0.091	0.05908
	Mat_t (s)	176	208	516
	Sol_t (s)	2	2	2
$u=$quadratic-1	Err_q (%)	0.01355	0.03865	0.02179
	Mat_t (s)	177	210	510
	Sol_t (s)	2	2	2
$u=$quadratic-2	Err_q (%)	0.03552	0.06985	1.091
	Mat_t (s)	176	211	516
	Sol_t (s)	2	2	2
$u=$cubic	Err_q (%)	0.02694	0.1203	1.638
	Mat_t (s)	176	210	513
	Sol_t (s)	2	2	2

still acceptable. The CPU time for constructing the matrices is independent of the field being solved but increases as the mesh becomes irregular. The reason for this is that in the cases of irregular node distribution, the nearly singular integration occurs when a source node falls into the adjacent cell of the integration cell, even though the geometry of this example is not a thin structure. The CPU time for solving the equation is kept constant in all cases. This is reasonable as the numbers of nodes for all the meshes are the same. The nearly singularity has been dealt with by scheme described in Section 4.1. This example clearly demonstrates the robustness of our method.

5.3. Dirichlet problems on an elbow pipe

In order to show the advantages of the meshless nature of the BFM, a problem with more complicated geometry is solved here. The geometry and its main dimensions are shown in Figure 9. Three sets of nodes, (a) 192 nodes, (b) 334 nodes, and (c) 523 nodes, have been used to obtain the numerical solutions. The node distribution and integration cells are shown in Figure 10. When the number of nodes distributed along one direction in the parametric space of a surface is less than 4, the variables on the surface are interpolated by the mixed interpolation scheme described in Section 2. Dirichlet boundary conditions according to the analytical solutions (Equations (31)–(34)) are imposed on all faces of the elbow pipe. The elbow pipe is a thin shell structure, thus, nearly singular integrals arises, which has been evaluated by the scheme described in Section 4.1. The L_2 errors of nodal values of q (denoted by Err_q) and time required for constructing the coefficient matrices (denoted by Mat_t) for various analytical fields are displayed in Table IV. Again, the CPU time is independent of the solved field and increases as more nodes are used. Numerical results of the normal flux q along the middle ring (see Figure 9) for the cubic analytical field (Equation (34)) are shown in Figure 11. It is seen that the numerical results obtained with the node sets (b) and (c) are in good agreement with the exact solutions. It should be pointed out that the preparation of the input data for this problem is very simple. Only eight panels on the

DOI: 10.1002/nme

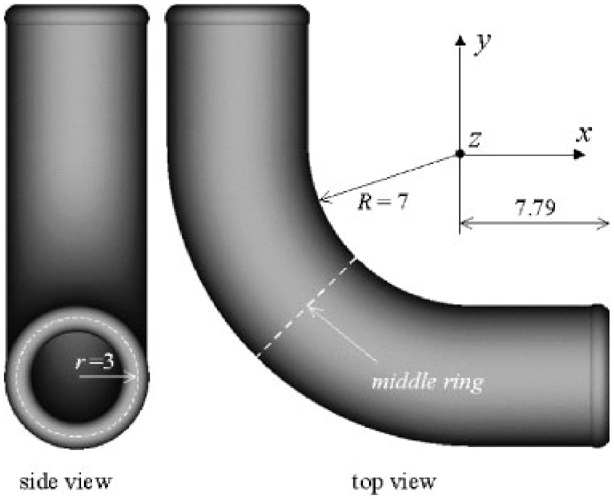

Figure 9. An elbow pipe and its main dimensions.

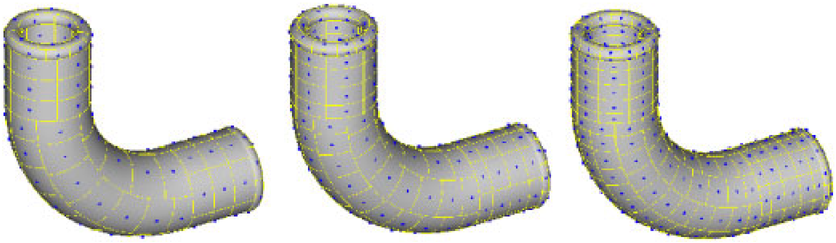

Figure 10. Node distribution and integration cells on an elbow pipe.

Table IV. Variation in L_2 error of q obtained by different sets of nodes for Dirichlet problems on an elbow pipe and timing results.

	Number of nodes	192	334	523
u = linear	Err_q (%)	2.232	0.9633	0.7815
	Mat_t (s)	14	37	80
u = quadratic-1	Err_q (%)	1.458	0.6227	0.4624
	Mat_t (s)	14	36	80
u = quadratic-2	Err_q (%)	2.114	0.7647	0.5919
	Mat_t (s)	13	37	80
u = cubic	Err_q (%)	2.135	0.7998	0.5462
	Mat_t (s)	13	36	80

DOI: 10.1002/nme

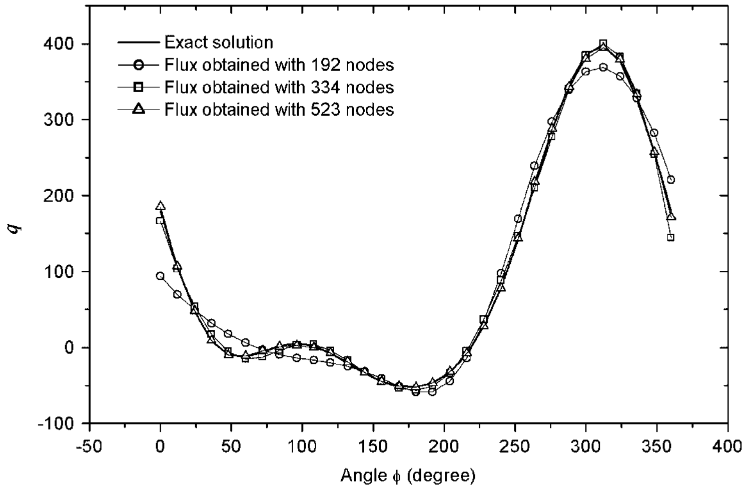

Figure 11. Normal flux, q, along the middle ring of an elbow pipe.

surface of the elbow pipe are defined and the boundary nodes and integration cells are generated automatically. The BFM is flexible and convenient, and could be an important step toward automatic simulation.

6. CONCLUSIONS

A BFM has been proposed for solving 3D potential problems. The method provides a new implementation of the BNM. In this new implementation, no elements are used for boundary integration or geometric approximation. Boundary integrations are performed using background cells, which are very easy to construct using only the isocurves in the parametric space of each boundary face. The integral quantities, such as the coordinates of Gaussian points, the Jacobian, and the out normal are calculated directly from the faces to avoid geometric errors. A mixed variable interpolation scheme of 1-D MLS and Lagrange Polynomial for long and narrow faces and an adaptive integration scheme for nearly singular integrals have been developed.

The BFM has been verified through a number of numerical examples with different geometries, boundary condition types and known analytical fields. It was observed that the solution is accurate for the potentials and fluxes on the boundary and inside the domain. High rates of convergence have been achieved. Our method can not only provide much more accurate results than the BNM, but also keep reasonable accuracy in some extreme cases, such as very irregular distribution of nodes and thin shell structures.

The BFM needs only the parametric representation of the surface of a body. As the parametric representation of created geometry is used in most of CAD packages, it should be possible to exploit their Open Architecture features, and automatically obtain required coefficients (representation). Therefore, the BFM has real potential to seamlessly interact with CAD software. Coupling the BFM with CAD software to handle arbitrary trimmed surfaces is an ongoing work.

By coupling with the FMM [12–14], the BFM may be able to perform large-scale computations for complicated structures. This is planned in the near future.

ACKNOWLEDGEMENTS

This work is supported by the National Science Foundation of China under grants 10725208, 60635020 and 50625519.

REFERENCES

1. Nayroles B, Touzot G, Villon P. Generalizing the finite element method: diffuse approximation and diffuse element. *Computational Mechanics* 1992; **10**:307–318.
2. Belytchko T, Lu YY, Gu L. Element free Galerkin methods. *International Journal for Numerical Methods in Engineering* 1994; **37**:229–256.
3. Zhu T, Zhang J, Atluri SN. A local boundary integral equation (LBIE) method in computation mechanics, and a meshless discretization approach. *Computational Mechanics* 1998; **21**:223–235.
4. Atluri SN, Zhu T. A new meshless local Petrov–Galerkin approach in computational mechanics. *Computational Mechanics* 1998; **22**:117–127.
5. Mukherjee YX, Mukherjee S. The boundary node method for potential problems. *International Journal for Numerical Methods in Engineering* 1997; **40**:797–815.
6. Chati MK, Mukherjee S. The boundary node method for three-dimensional problems in potential theory. *International Journal for Numerical Methods in Engineering* 2000; **47**:1523–1547.
7. Zhang JM, Yao ZH, Li H. A hybrid boundary node method. *International Journal for Numerical Methods in Engineering* 2002; **53**:751–763.
8. Zhang JM, Yao ZH. Meshless regular hybrid boundary node method. *Computer Modeling in Engineering and Sciences* 2001; **2**:307–318.
9. Zhang JM, Yao ZH, Tanaka M. The meshless regular hybrid boundary node method for 2-D linear elasticity. *Engineering Analysis with Boundary Elements* 2003; **27**:259–268.
10. Zhang JM, Yao ZH. Analysis of 2-D thin structures by the meshless regular hybrid boundary node method. *Acta Mechanica Sinica* 2002; **15**:36–44.
11. Hughes TJR, Cottrell JA, Bazilevs Y. Isogeometric analysis: CAD, finite elements, NURBS, exact geometry and mesh refinement. *Computer Methods in Applied Mechanics and Engineering* 2005; **194**:4135–4195.
12. Zhang JM, Tanaka M, Endo M. The hybrid boundary node method accelerated by fast multipole method for 3D potential problems. *International Journal for Numerical Methods in Engineering* 2005; **63**:660–680.
13. Zhang JM, Tanaka M. Fast HdBNM for large-scale thermal analysis of CNT-reinforced composites. *Computational Mechanics* 2008; **41**:777–787.
14. Zhang JM, Tanaka M. Adaptive spatial decomposition in fast multipole method. *Journal of Computational Physics* 2007; **226**:17–28.
15. Nagaranjan A, Mukherjee S. A mapping method for numerical evaluation of two-dimensional integrals with 1/r singularity. *Computational Mechanics* 1993; **12**:19–26.
16. Liu YJ. Analysis of shell-like structures by the boundary element method based on 3-D elasticity: formulation and verification. *International Journal for Numerical Methods in Engineering* 1998; **41**:541–558.
17. Chen JT, Hong HK. Review of dual boundary element methods with emphasis on hypersingular integrals and divergent series. *Applied Mechanics Reviews* 1999; **52**(1):17–33.

DOI: 10.1002/nme